Inelastic Neutron Scattering for Neel Phase Excitation Spectrum of SrCu$_2$(BO$_3$)$_2$

TP4 by Martin T. Bruland[1,2], supervised by Ellen Fogh[1] and Henrik M. Rønnow[1]

[1]Laboratory of Quantum Magnetism, Ecole Polytechnique Federale de Lausanne.

[2]Department of Physics, Norwegian University of Science and Technology

January, 2023

Abstract

Spin excitations in the antiferromagnetic Néel phase of the Shastry-Sutherland crystal SrCu$_2$(BO$_3$)$_2$ have been investigated using inelastic neutron scattering. No clear excitations could be identified, possibly due to challenging experimental conditions ultimately leading to mechanical failure of the sample environment. Characteristic excitations from a Rollin film of superfluid helium were observed, as the weakest signal yet identified at the CAMEA SINQ instrument.

Introduction

The compound SrCu$_2$(BO$_3$)$_2$ has been of interest since it was realized that its magnetic structure is well described by a frustrated 2D spin model, investigated analytically by Shastry and Sutherland[1] in 1981. An antiferromagnetic Néel state is theoretically predicted as ground state at certain conditions, and a phase transition has previously been observed[2] at low temperature ($\sim 4\,\mathrm{K}$) and high pressure ($\sim 3\,\mathrm{GPa}$). This study has attempted to investigate the Néel phase through inelastic neutron scattering, with the aim of determining the spin excitations of this phase and to compare this with known antiferromagnetic excitations. As the experimental conditions remain challenging, experimental considerations including cooling and pressure determination are included for future experiments.

Crystal and Spin Model

SrCu$_2$(BO$_3$)$_2$, also known as SCBO, holds a tetragonal crystal structure (space group $I\bar{4}2m$) with a conventional unit cell of $Z = 4$ formula units having lattice parameters of[3] $a = 8.995\,\text{Å}$ and $c = 6.649\,\text{Å}$.

The magnetic properties of SCBO arise from Cu^{2+} ions with unpaired electrons, found in planes normal to the **c**-direction, as shown in Fig. 1a. These ions are found pairwise in dimers, and the magnetic interactions are understood to be dominated by inter- and intradimer superexchange interactions, J and J' respectively as indicated in Fig. 1b, which arise from in-plane bonds to oxygen and boride groups. A Heisenberg model
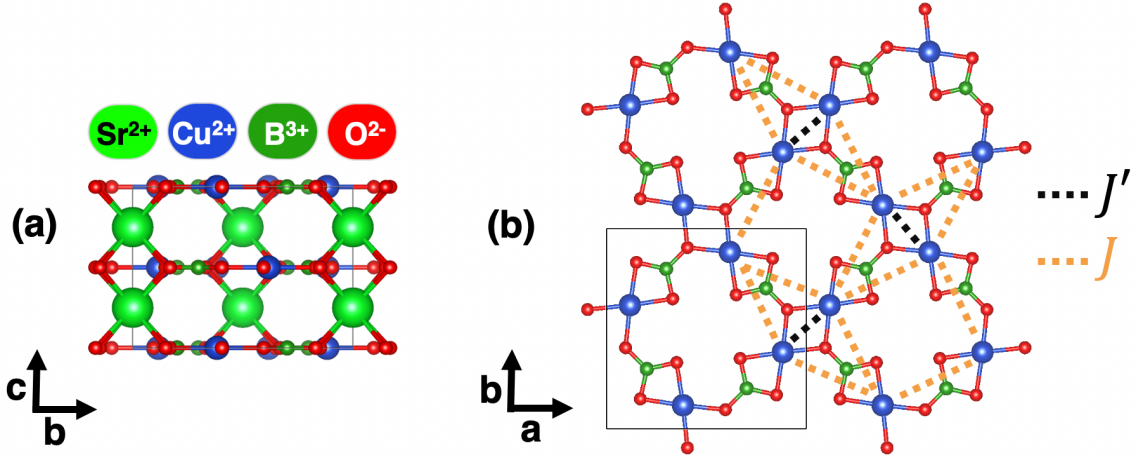
Figure 1: Crystal structure of SCBO with black square indicating the $Z = 4$ unit cell. (a) The copper ions are found in layers normal to $\mathbf{c}$ (b) J and J' interactions are found in ab planes. Figures made using *VESTA*[4], and atomic positions from *The Materials Project*[5].

with these spin-isotropic interactions would lead to a continuous symmetry of spin-rotation, so the Mermin-Wagner theorem[6] would not permit long ranged magnetic order at non-zero temperatures due to the 2D nature of the system. However, interplanar exchange interactions and Dzyaloshinskii–Moriya (DM) interactions have been proposed to be significant.[7] In addition, an in-plane intradimer DM interaction has been observed[3] with a strength at the scale of $D \approx 0.03J$.

If considering only the J and J' interactions, the spin system is topologically equivalent to the Shastry-Sutherland model[1], illustrated in Fig. 2a. Its ground state is dependent on the ratio $\alpha = J/J'$. This ratio is tuned experimentally by applying pressure, altering bond angles and thus changing the strength of the exchange interactions. In the limit of large α, a Néel ground state is expected[1] where the vanishing intradimer interactions allow for parallel neighbouring spins (i.e. parallel triplet states within each dimer), while antiferromagnetic order
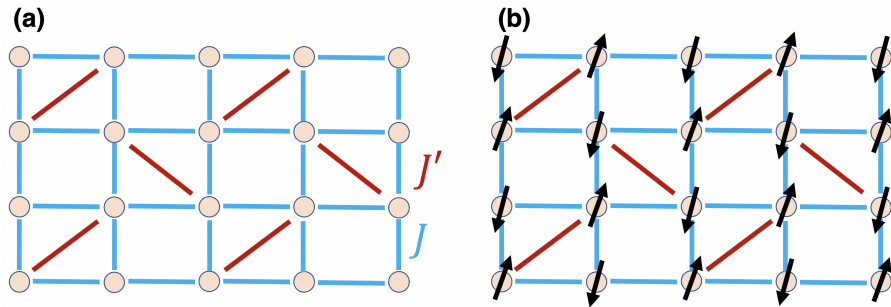

Figure 2: (a) Shastry-Sutherland model (b) Néel state. Note that ions linked by J' are nearest neighbours while J is the interdimer interaction in the physical system.
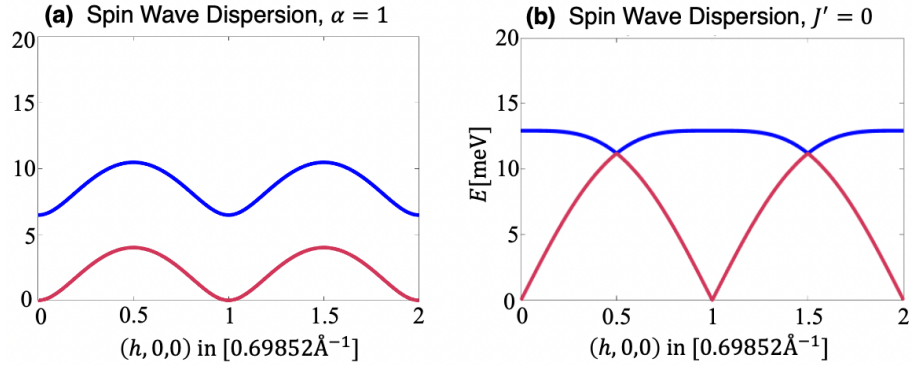
2

Figure 3: Spin wave calculations of SCBO considering only J and J' interactions. (a) Spin wave dispersions along $(h, 0, 0)$ using $J = 75\,\mathrm{K}$ and $\alpha = 1$ (b) Spin wave dispersions along $(h, 0, 0)$ using $J = 75\,\mathrm{K}$ and $J' = 0$.

is fully satisfied for the interdimer interaction, illustrated in Fig. 2b. In the limit of small α, the ground state is found to consist of singlet states at every dimer, while there seems to exist an intermediate plaquette state where four sites jointly occupy a singlet state. A transition from the plaquette phase to the Neél phase has been calculated to occur at[8] $\alpha = 0.765$, and this has been experimentally realized[2] using a pressure of $P \approx 3\,\mathrm{GPa}$. In order to observe the Néel phase, one should be cautious of a structural monolinic transition[9] at $P \sim 4\,\mathrm{GPa}$.

Numerical spin-wave calculations have been performed using the software SpinW[10], considering only J and J' interactions and thus neglecting all inter-layer and DM interactions. The interaction strength was set to $J = 75\,\mathrm{K}$, $\alpha = 1$, and the spin wave dispersions were obtained through the Copla[11] method, as implemented in SpinW. The energy scale is a rough estimate as it would change as function of pressure, but interactions of this order of magnitude have been reported[2]. Using $\alpha < 1$ did not yield successful simulations due to the software not accepting the Néel state as the true ground state at $\alpha < 1$.

As shown in Fig. 3a, two branches separated by a gap were found. The lowest energy branch is non-linear in the low q regime, as opposed to the square lattice unfrustrated antiferromagnet. For comparison, a similar calculation was performed with $J' = 0$, thus lifting frustration, and the low energy branch is now linear in the small q limit, as shown in Fig. 3b.

Due to the uncertainty in energy scale and several interactions being neglected, these spin wave calculations should not be trusted to accurately describe the system. They do however indicate that in the physical system, we might expect excitations distinctly different than those in an unfrustrated antiferromagnet, in spite of identical ground states.

Experimental Setup

A single crystal of SCBO was cut along the plane (001) to produce a sample of mass $39.2\,\mathrm{mg}$ with the **c**-direction pointing out of the scattering plane. The sample height along **c** was $1.90\,\mathrm{mm}$, and the remaning directions fit in a cylinder of radius of $3\,\mathrm{mm}$. This small sample size was required from the size of the pressure cell. Small size should limit second-order scattering effects but it also yields a weak scattering signal, requiring long exposure time to differentiate any signal from background noise. Laue X-ray diffraction was performed to verify the crystal directions, and the (001) plane was identified at the flat cut face.

To enable applying isotropic pressure, the crystal was encapsulated in grated lead powder, which was compacted by a pressure of $3.5\,\mathrm{tons}$ in a hydraulic press, and concealed in a gasket of TiZr and BeCu. This encapsulation aids in transferring stress isotropically to the crystal. To apply pressure inside the neutron spectrometer, the gasket would be stationed between two anvils inside a Paris-Edinburgh pressure cell.

An additional alignment test was performed in a neutron diffraction instrument to determine the crystallographic directions in relation to the gasket. This was done with the gasket placed between the anvils to ensure that sufficient tilt to mitigate potential misalignment of the **c**-axis would be possible without the anvils blocking the neutron path.

Inelastic neutron scattering was performed at the triple-axis multiplexing CAMEA[12] instrument at the Swiss Spallation Neutron Source (SINQ). Since neutrons have no charge, they interact weakly with materials and most neutrons pass through the instrument without scattering off neither the sample nor the sample environment, allowing us to measure the sample inside the gasket, required for applying the isotropic pressure. At the same time, the neutron spin makes them scatter from magnetic fields in the sample, enabling observation of the sample spin structure. The instrument is supplied with cold neutrons and has 8 analyzers with intensity profiles as shown in Fig. 4. This in addition to position sensitive detectors allows for observing several energy transfers at a range of scattering angles simultaneously. The data was treated using the neutron scattering software MJOLNIR[13]. To achieve the desired sample environment, a the PE pressure cell and a closed cycle cryostat assisted with liquid helium were used.
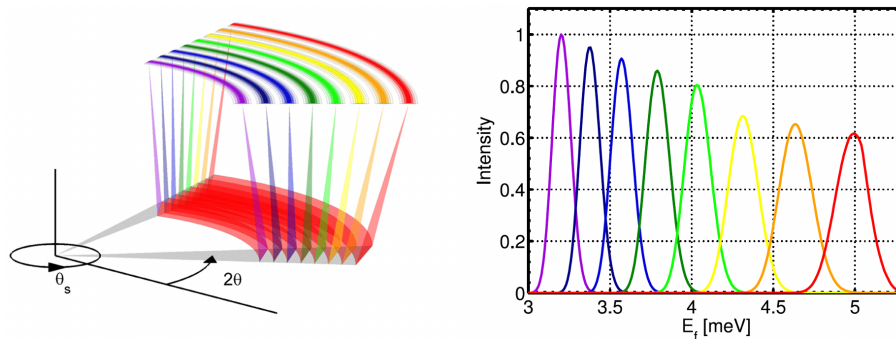

Figure 4: CAMEA schematic and analyzer intensities. Figures gathered from Groitl *et al.*[12]

Pressure Determination

The pressure delivered to the sample through the pressure cell is not probed directly, so the pressure was investigated by observing elastic scattering from lead in the sample gasket. The lattice parameter of lead is known as function of pressure and temperature through an equation of state. Thus, observing the lattice parameter will determine the applied pressure. The lattice parameter is determined from Bragg's Law:

$$2d \sin \theta = n\lambda,$$

where d is the spacing of scattering planes, θ is the incident angle which is half of the scattering angle, the integer n is the scattering order and λ is the wavelength of the scattered species, in this case neutrons.

For the pressure determination, we used neutrons of initial energy $E_i = 5\,\text{meV}$, corresponding to a de Broglie wavelength of:

$$\lambda = \frac{h}{\sqrt{2m_n E_i}} = 4.045\,\text{Å},$$

using the Planck constant h and the neutron mass m_n.

The lead in the gasket is polycrystalline, so scattering from identical scattering planes will occur in different directions in the different grains of the material. To combine the scattering signal from different directions, increasing the available data compared to a single scattering direction, a powder average was performed, where for each magnitude of the scattering vector $\mathbf{q}$, the intensity is averaged over all scattering directions. Lead has an fcc crystal structure[14]. The (111) scattering peak of lead was identified, as it is the first visible diffraction peak according to the face centered selection rule, requiring h, k and l to be all even or odd[15]. For a cubic crystal system, the lattice spacing is in general $d_{khl} = a/\sqrt{h^2 + k^2 + l^2}$, so for the (111) scattering plane, $d_{111} = a/\sqrt{3}$. Thus, the lattice parameter can be determined by:

$$a = \frac{\sqrt{3}\lambda}{2 \sin \theta}$$

A reference measurement was done at ambient conditions, yielding a diffraction peak at $2\theta = 90.26°$ and a lattice parameter of $a_0 = 4.9426\,\text{Å}$, used as a reference for the equation of state. After applying pressure and cooling the sample to $6.5\,\text{K}$, the peak was found at $2\theta = 93.70°$, giving a smaller lattice parameter of $a = 4.8013\,\text{Å}$. Using the equation of state found by Strässle et al[16], the pressure was calculated to $P = 3.8\,\text{GPa}$, which should be below the monoclinic transition[9] and above the transition to the Néel phase[2] in the $T \approx 2\,\text{K}$ range. The pressure is not expected to change significantly by further cooling to $1.7\,\text{K}$.

Cooling

In order to reach a temperature below $2\,\mathrm{K}$, a closed cycle cryostat had to be enhanced by filling the sample space with liquid helium. The temperature lowers further than the liquid helium temperature due to helium vaporizing in the cryostat. After filling, characteristic phonons, maxons and rotons are observed until enough liquid helium is evaporated so it no longer covers the sample. Observed helium excitations after cooling are shown in Fig. 5a, which align well with previous observations of helium excitations[17].

Given a liquid helium density of $0.13\,\mathrm{g/cm^3}$ and initial neutron energy of $E_i = 4\,\mathrm{meV}$, the penetration depth of neutrons[18] is $37\,\mathrm{cm}$. This implies that $10\,\mathrm{cm}$ of liquid helium along the path of the neutrons (the technical drawing of the pressure cell indicates $\approx 5\,\mathrm{cm}$ before and after the sample) would absorb roughly $1 - e^{-10/37} \sim 25\%$ of the neutron beam, significantly obstructing any scattering signal. Thus, it was of interest to determine how much waiting time was required after the filling process until enough liquid helium is vaporized to not cover the neutron trajectory, and measurement can be resumed.

In order to determine the required waiting time, we investigated the time dependence of the intensity from the $(\bar{2}00)$ Bragg peak of SCBO. We also looked at the intensity integrated over the inelastic regime, which was found to be dominated by scattering from helium. The results, as shown in Fig. 5b imply a required waiting time of $6\,\mathrm{h}$, corresponding to a sharp decrease in inelastic scattering. We also observe a sharp increase in Bragg peak intensity, where the muted level from the helium is in accordance with the estimated 25% reduction.

To decrease the waiting time after filling, heaters in the sample environment were tested to see if they could provide faster helium evaporation without significantly reducing the time of which the sample has an acceptable temperature $< 1.8\,\mathrm{K}$, thus increasing the available measurement time of the experiment. A comparison of waiting time using no heating, $0.5\,\mathrm{W}$ and $1\,\mathrm{W}$ heating is shown in Fig. 6. To synchronize the start time of the measurements, the temperature evolutions were compared. Due to different temperature curves from different
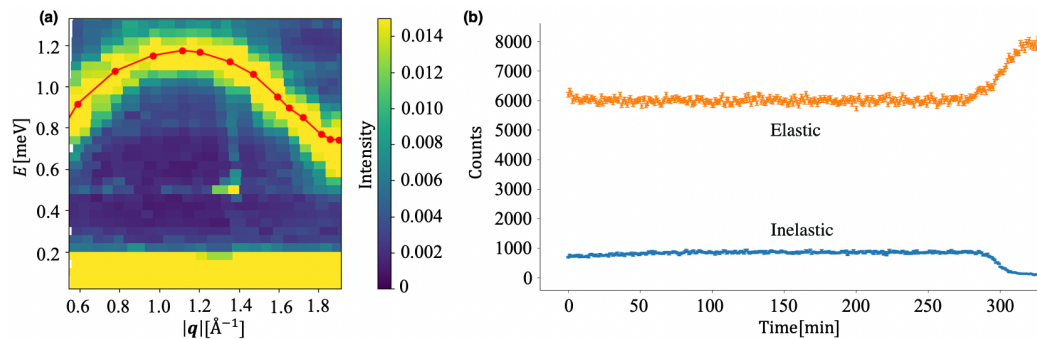

Figure 5: Cooling process using liquid helium (a) Helium excitations observed after filling. Dotted curve is experiment by Bobrov et al.[17] (b) Time evolution of scattering intensity after cooling. $6\,\mathrm{h}$ was found as sufficient waiting time without using sample environment heaters.
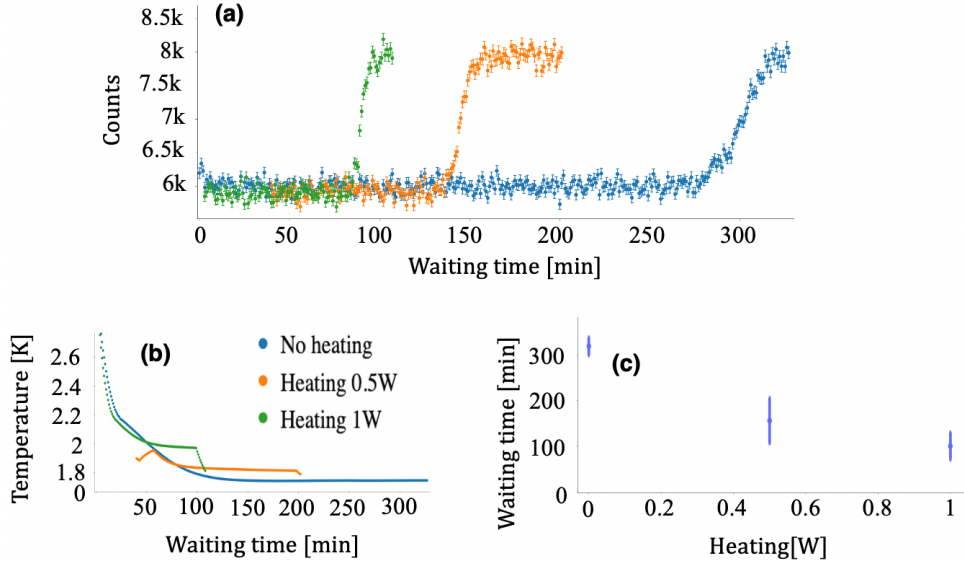
Figure 6: Waiting time of cooling process is reduced through heaters. (a) Intensity of ($\bar{2}$00) Bragg peak as function of time (b) Temperature evolutions (c) Required waiting time decreases with heating.

heating and different initial temperatures, this alignment is rough and gives large uncertainty in the waiting time. There is however a trend where more heating seems to provide shorter waiting times. Heating of 1 W for 1.5 h was found to blow off enough helium so it no longer covers the sample, drastically reducing the waiting time, while still providing a long cold time of 13.5 h, compared to ≈ 15 h without heating. We note that the heater can delay the temperature drop below 1.8 K, increasing the waiting time to around 2 h for 1 W, so there seems to be a trade-off. Using 1 W was found to allow for ideally performing measurements roughly 80% of the beam time, accounting for 1 h of performing the filling procedure.

Background Measurement

A measurement was performed at $T = 6.5$ K and $P = 3.8$ GPa in order to measure the background signal from the sample in paramagnetic phase and the sample environment, which we later could subtract from the low-T measurement. This allows for identifying weaker signals in the low-T measurement after subtracting the background, but also prevents any background scattering signals from being interpreted as excitations of the Néel phase.

Elastic Bragg peaks were found at positions ($\bar{1}$10), ($\bar{2}$00), and ($\bar{3}$10), as shown in Fig. 7a, satisfying the reflection condition $h + k + l = 2n$ of the $I\bar{4}2m$ space group[19]. A masking tool was used to be able to distinguish the scattering from the Bragg peaks from the rest of the background scattering. A region of low signal is observed due to blocking from the pillars of the pressure cell, and it resembles a simulation shown in Fig. 7b.
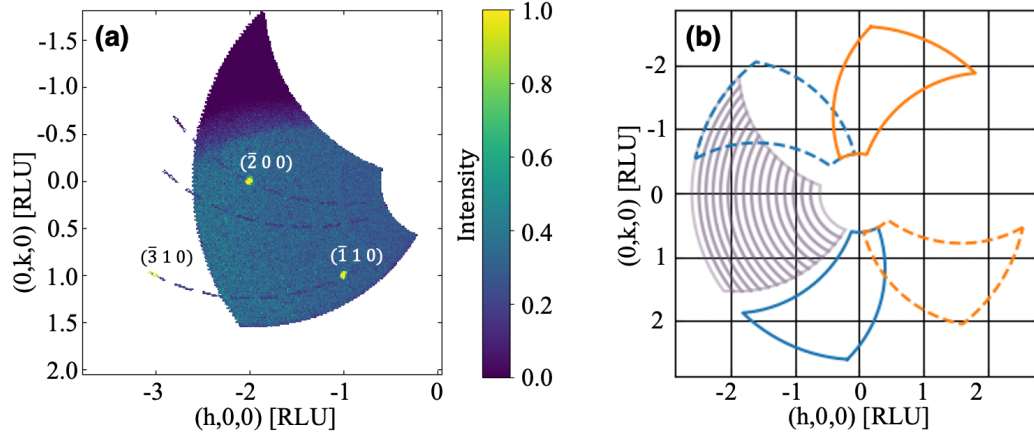
Figure 7: (a) Elastic background scattering. Bragg peaks are identified at $(\bar{1}10)$, $(\bar{2}00)$, and $(\bar{3}10)$ (b) Simulation of pillars of the pressure cell (blue and orange elements) obstructing a region of the measurable reciprocal space (striped element) of elastic scattering.

The scattering intensity was investigated as a function of scattering vector $\mathbf{Q}$ and energy transfer E by performing a cut along direction $[h00]$, cutting through the Bragg peak $(\bar{2}00)$. As shown in Fig. 8a, both the Bragg peak and the remaining background, found by applying the masks, seem to have a peak centered near $E = 0$. By curve-fitting the data to a Gaussian altered by a slope, the Bragg peak at $(\bar{2}00)$, was found to be centered at $\mu = (0.00251 \pm 0.0007)\,\mathrm{meV}$ with a standard deviation of $\sigma = (0.03204 \pm 0.0007)\,\mathrm{meV}$, as shown in Fig. 8b. For the total background signal excluding the Bragg peaks, the curve in Fig. 8c is centered at $\mu = (-0.00224 \pm 0.0001)\,\mathrm{meV}$ and has a width of $\sigma = (0.04789 \pm 0.0002)\,\mathrm{meV}$. This implies successful alignment of the sample, and an energy resolution on order of $\delta E = \mathrm{FWHM} \sim 0.1\,\mathrm{meV}$ which is larger than the offset from $E = 0$. The magnitude of incoherent scattering, in this case total scattering intensity without the Bragg peaks, is $\sim 35\%$ of vanadium, which is often used as a reference for neutron scattering.

There are instrument-related background fluctuations on the magnitude of 0.1% of that of vanadium, as shown in Fig. 8d. The largest fluctuations, with peaks such as $\approx 2.7\,\mathrm{meV}$ and $\approx 4.8\,\mathrm{meV}$ oscillate with a wavelength corresponding to the energy span of the 8 analyzers of the CAMEA instrument, Fig. 4. There are also shorter oscillations corresponding to the different analyzers.

Since the background except for the Bragg peaks is isotropic, as Fig. 7a suggests, the Bragg peaks were masked out and the remaining background was transformed to a powder average to again have more observations per scattering event. The resulting powder average is shown in Fig. 9. The background intensity seems to increase with $|\mathbf{q}|$.
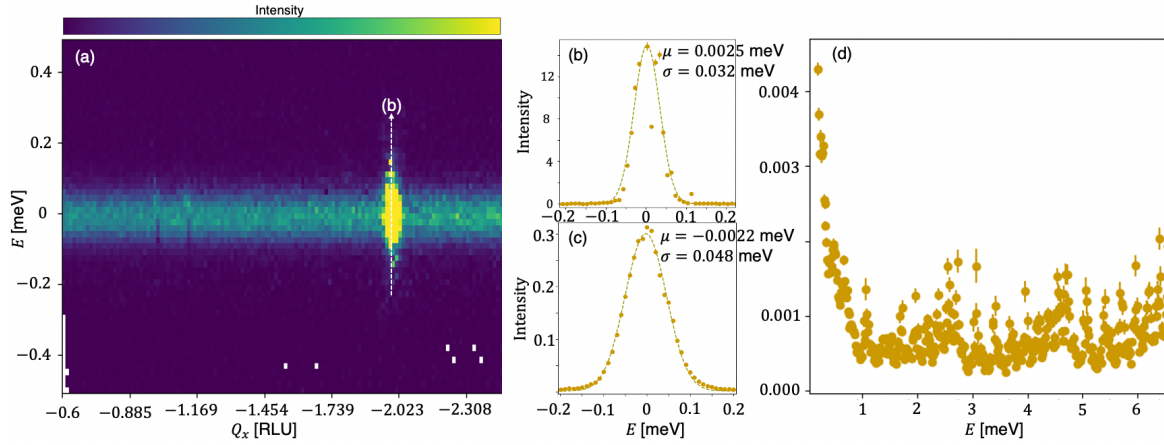
Figure 8: Background measurement at $6.5\,\mathrm{K}$ and $3.85\,\mathrm{GPa}$. **(a)** Scattering intensity, in units of vanadium, as a function of energy transfer along a cut $[h00]$ cutting the $(\bar{2}00)$ Bragg peak. **(b)** Scattering intensity, in units of vanadium, as function of energy transfer at the Bragg peak $(\bar{2}00)$ **(c)** Incoherent scattering, averaged over $\mathbf{Q}$ excluding the Bragg peaks. **(d)** Systematic intensity fluctuations from instrumental setup on the order of 0.1% of vanadium, averaged over $\mathbf{Q}$ excluding the Bragg peaks.
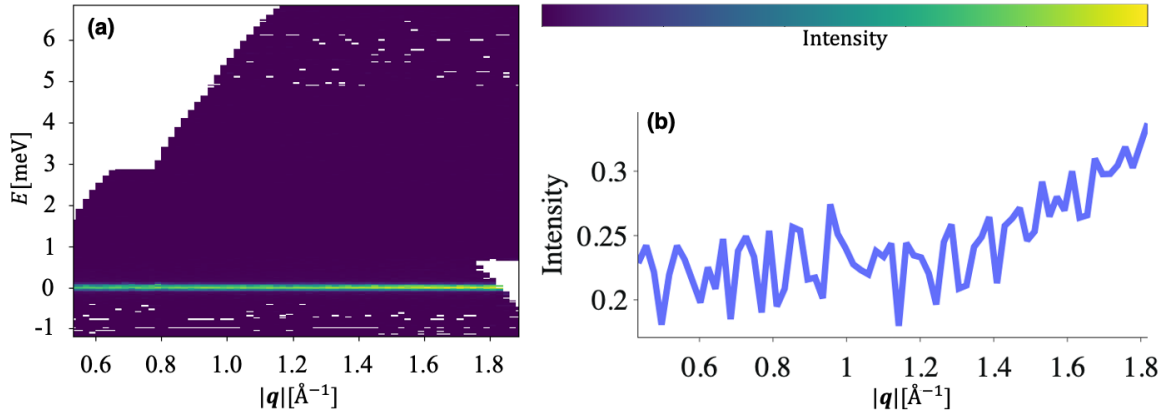

Figure 9: (a) Powder averaged background with Bragg peaks masked out. This would be subtracted from the low-T measurement. (b) Intensity of elastic band as function of $|\mathbf{q}|$, normalized with respect to vanadium.

9

Results

The main scattering measurement was performed at $T = 1.7\,\mathrm{K}$ and $P = 3.8\,\mathrm{GPa}$. Again the same Bragg peaks were identified and masked out, and the powder averaged background measurement was subtracted.

Cuts along different directions in $\mathbf{Q}$, with the powder-averaged background subtracted, are shown in Fig. 10, but no clear sample signals could be identified.

A powder average, as shown in Fig. 11 shows helium excitations although measurements were performed after enough liquid helium was evaporated to not cover the sample. The intensity is not constant along the dispersion relation as it was for the liquid helium in Fig. 5a, but strongest near the minimum at $|\mathbf{q}| \approx 2\,\mathring{\mathrm{A}}^{-1}$. This nonuniform intensity is consistent with scattering from superfluid helium excitations[20], implying a Rollin film[21] of superfluid helium creeping up the surfaces of the sample environment due to the Onnes effect.

In addition to the helium excitations near $E = 1\,\mathrm{meV}$, the powder average seems to show some increased scattering in the range between 6 and 7 meV. This is supported by investigating scattering intensity as function of energy transfer, Fig. 11d, normalized with respect to vanadium.

Discussion

Surprisingly, no clear excitations were identified in the $\mathbf{Q}$-cuts. One explanation could be that there are no excitations in the range we measured, or that their scattering amplitude is too weak to be observed with the given beam time. Observing scattering from a Rollin film of thickness on the order of only $\sim 10 - 100\,\mathrm{nm}$[22] indicates that weak scattering signals can be observed when subtracting the background signal, but the anisotropy of this scattering amounts to all scattering directions contributing to the same signal in the powder spectrum, making it easier to detect.

Another possibility could be that the sample was not in the Néel phase, either that some condition made
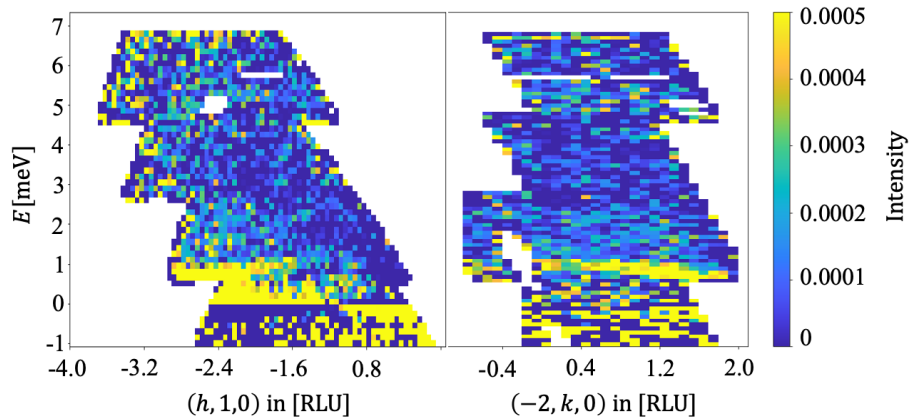

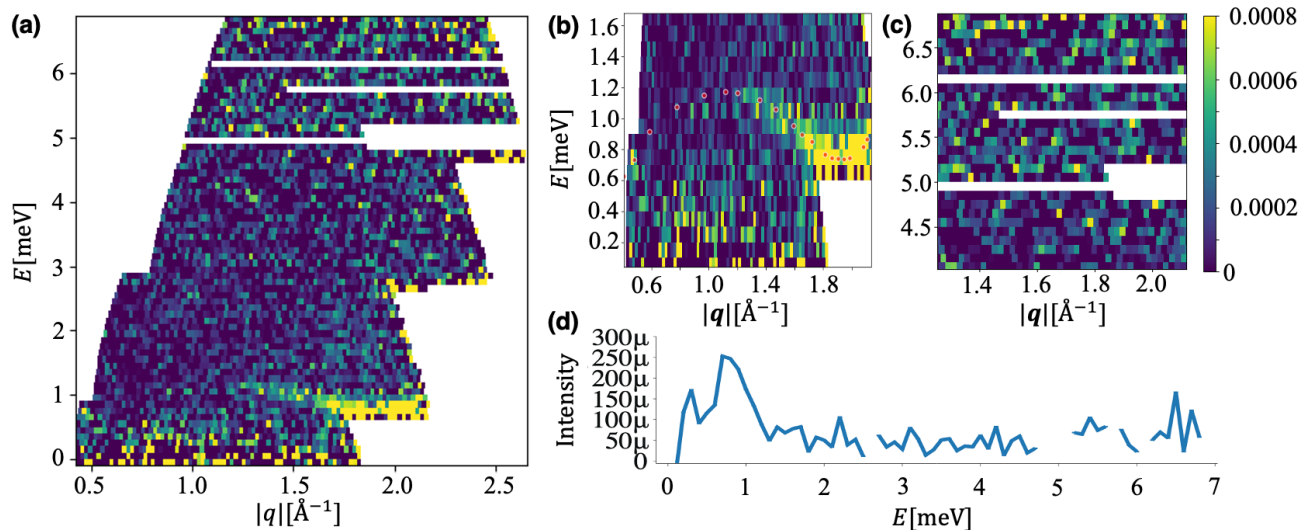Figure 10: Cuts in k-space. No clear excitations are identified.

Figure 11: Powder average of low-T measurement. (a) Complete powder spectrum (b) Helium excitations, red dots from experiment by Bobrov et al.[17] (c) Increased scattering at high energy transfers (d) Normalized intensity as function of energy transfer. An increase is found between 6 and 7 meV.

a pressure of 3.8 GPa insufficient to reach the Néel phase, or that the actual pressure was different than the calculation. Due to rigid lattice parameters of SCBO, these were not used for pressure determination, but this could possibly be used as a secondary measurement to rule out this explanation. Since the results show cancellation of the same scattering peaks in accordance with space group $I\bar{4}2m$, the monoclinic transition did not occur, so the pressure should not have been too high. Mechanical failure of the anvils of the pressure cell prevented measuring at higher pressure.

There seems to be some increased scattering in the range of 6 to 7 meV compared to the background, although no clear dispersion relations are identified. Judging by the fluctuations of Fig. 11d, its is unclear if this is a definite increase or a statistical error, but if there is an increase, it could arise from the sample in the Néel phase. In this case, further measurement in this energy range could be interesting, as excitiations in this range could possibly give stronger scattering amplitude. If there exists a low-gradient branch in this region, a high density of states could explain a strong scattering amplitude. Another possibility, although less plausible, is that this scattering originates from a second branch of superfluid helium excitations, but no such excitations seem to have been previously reported.

The experimental setup using the CAMEA instrument and the sample evniroment seems to be able to detect small signals, even from a thin film of helium, enable high precision sample alignment and yield high beam time efficiency.

Conclusion

No clear excitations could be identified in the Néel phase of SCBO in our experiment. In stead, we observed the excitation spectrum of superfluid helium. A possible strategy for further experiments based on the results of this study could be measuring more at energy transfers in the range of 6 to 7 meV, and if possible, find a complementary method of determining the applied pressure to ensure that the desired pressure is indeed reached.

References

1. Shastry, B. S. & Sutherland, B. Exact Goundstate of a Quantummechanical Antiferromagnet. *Physica* **108B** (1981).

2. Guo, J. *et al.* Quantum phases of SrCu2(BO3)2 from high-pressure thermodynamics. *Phys. Rev. Lett.* **124** (2020).

3. Kodama, K. *et al.* Field-induced effects of anisotropic magnetic interactions in SrCu2(BO3)2. *J. Phys.: Condens. Matter* **17** (2005).

4. Momma, K. & Izumi, F. VESTA 3 for three-dimensional visualization of crystal, volumetric and morphology data. *J. Appl. Crystallogr.* **44** (2011).

5. Jain, A. *et al.* Commentary: The Materials Project: A materials genome approach to accelerating materials innovation. *APL Mater.* **1.** https://materialsproject.org/materials/mp-558472/ (2013).

6. Mermin, N. D. & Wagner, H. Absence of Ferromagnetism or Antiferromagnetism in One- or Two-Dimensional Isotropic Heisenberg Models. *Phys. Rev. Lett.* **17** (1966).

7. Haravifard, S. *et al.* Emergence of long-range order in sheets of magnetic dimers. *PNAS* **111** (2014).

8. Corboz, P. & Mila, F. Tensor network study of the Shastry-Sutherland model in zero magnetic field. *Phys. Rev. B* **87** (2013).

9. Zayed, M. E. *et al.* Temperature dependence of the pressure induced monoclinic distortion in the spin S = 1/2 Shastry–Sutherland compound SrCu2(BO3)2. *Solid State Commun.* **186** (2014).

10. Toth, S. & Lake, B. Linear spin wave theory for single-Q incommensurate magnetic structures. *J. Phys.: Condens. Matter* **27** (2015).

11. Copla, J. H. P. Diagonalization of the quadratic boson hamiltonian. *Physica A* **93** (1978).

12. Groitl, F. *et al.* CAMEA—A novel multiplexing analyzer for neutron spectroscopy. *Rev. Sci. Instrum.* **87** (2016).

13. Lass, J. *et al.* MJOLNIR: A Software Package for Multiplexing Neutron Spectrometers. *SoftwareX* **12** (2020).

14. WebElements. *Lead: crystal structures* Visited: 10.01.2023. https://www.webelements.com/lead/crystal_structure.html.

15. Sands, D. E. *Introduction to Crystallography* (Dover Publications Inc., 1975).

16. Strässle, T., Klotz, S., Kunc, K., Pomjakushin, V. & White, J. S. Equation of state of lead from high-pressure neutron diffraction up to 8.9 GPa and its implication for the NaCl pressure scale. *Phys. Rev. B* **90** (2014).

17. Bobrov, V., Trigger, S. & Litinski, D. Universality of the Phonon–Roton Spectrum in Liquids and Superfluidity of 4He. *Z. Naturforsch. A* **71** (2016).

18. For Neutron Research, N. C. *Neutron activation and scattering calculator* Visited 26.11.2022. https://www.ncnr.nist.gov/resources/activation/.

19. Department of Chemistry, U. C. L. *A Hypertext Book of Crystallographic Space Group Diagrams and Tables* Visited: 03.01.2023. 1999. http://img.chem.ucl.ac.uk/sgp/large/121az2.htm.

20. Glyde, H. R. Excitations in the quantum liquid 4He: A review. *Rep. Prog. Phys.* **81** (2017).

21. Rollin, B. V. & Simon, F. On the 'film' phenomenon of liquid helium II. *Physica* **6** (1939).

22. Jackson, L. C. & Burge, E. J. Thickness of the Helium II Film. *Nature* **164** (1949).